Zhang, L., S. Yang, X. Wang, K. Cai, J. Li, X. Wan, & B.G Thomas. AISTech 2004, Nashville, TN, Sep.15-17, 2004. Assoc. Iron Steel Technology, Warrendale, PA.

# Physical, Numerical and Industrial Investigation of Fluid Flow and Steel Cleanliness in the Continuous Casting Mold at Panzhihua Steel

Dr. Lifeng Zhang
Dept. of Mech. Engr., University of Illinois at Urbana-Champaign
1206 W. Green St., Urbana, IL 61801, USA
Phone number: 1-217-244-4656
Fax number: 1-217-244-6534
Email: zhang25@uiuc.edu

Dr. Subo Yang
Technical Research Center, Panzhihua Iron and Steel Company
Panzhihua, Sichuan Province, P.R.China
Phone number: 0086-812-3332932
Fax number: 0086-812-3336175

Xinhua Wang, Kaike Cai, Jiying Li, Xiaoguang Wan
School of Metallurgy, University of Science & Technology Beijing
Beijing 100083, P.R.China
Phone number: 0086-10-6233-2267
Email: wxhhome@public3.bta.net.cn

Brian G. Thomas
Dept. of Mech. Engr., University of Illinois at Urbana-Champaign
1206 W. Green St., Urbana, IL 61801, USA
Phone number: 1-217-333-6919
Fax number: 1-217-244-6534
Email: bgthomas@uiuc.edu

Key Words: Continuous Casting, SEN, Mold, Water Model, Computational Model, Fluid Flow, Level Fluctuation, Inclusions, Industrial Measurement

## INTRODUCTION

Fluid flow in the Submerged Entry Nozzle (SEN) and the continuous casting mold is important due to its effect on many phenomena related to the steel quality, such as the transport of argon bubbles and inclusions, transient fluctuations and waves at the top surface, the transport of superheat, meniscus freezing, shell thinning from the jet impinging upon the solidifying shell, thermal stress and crack formation. Extensive past work has employed physical water models to investigate fluid flow phenomena in the mold region of the continuous casting process. [1-16) 17)] The first study was carried out by Afanaseva et al [1)] for a straight bore nozzle system. Heaslip et al extensively studied the fluid flow in SENs under stopper-rod control and slide-gate control [5, 6)]. Gupta investigated the residence time distribution [7)], asymmetry and oscillation of the fluid flow pattern [8, 9)], and slag entrainment [10, 11)]. Tanaka et al [12)] and Wang et al [15)] studied the influence of wettability on the behavior of argon bubbles and fluid flow. Teshima et al [13)] and Iguchi et al [14)] studied slag entrainment. However, there are few papers with measurements of level fluctuations at the meniscus [13)] and other places of the top surface of the mold. Only a few papers investigate the impingement pressure on the narrow face, which affects solidification.

As shown in Figure 1, the causes of slag entrainment in the continuous casting mold include:

1) Turbulence and level fluctuations at the meniscus. If the jet from the SEN outport impinges on the narrow face and partly flows upwards along the narrow face, it lifts the level of the molten steel, and generates large level fluctuations near the meniscus. The slag there is pushed away from the narrow face as the surface flow direction reverses; [18-25)]

2) Periodic oscillations of the level induced by unsteady fluid flow in the mold, [26)] caused by flow problems such as uneven flow discharge from opposite ports of the SEN; [18)]

3) Vortices formed between the SEN and the narrow face, such as induced by the asymmetrical flow in the mold; [18, 27)]

4) Emulsification of the slag / steel interface, such as caused by the rupture of bubbles floating to this interface; [24, 28)]

5) Suction of steel down along the SEN wall due to flow recirculation and the low pressure region just above the SEN port exits. [18)] The mold slag can enter the upper portion of the ports and cause clogging problems, or become entrained into the jet, and cause serious slag entrainment.

6) Jet impingement onto the steel-slag interface associated with a single roll flow pattern, such as induced by excessive gas bubble injection. [29)]

Hence, the fluid flow pattern in the mold and level fluctuations are of great importance to slag entrainment quality problems. [30)] Large level fluctuations correlate with more surface defects in the steel product. [31)]

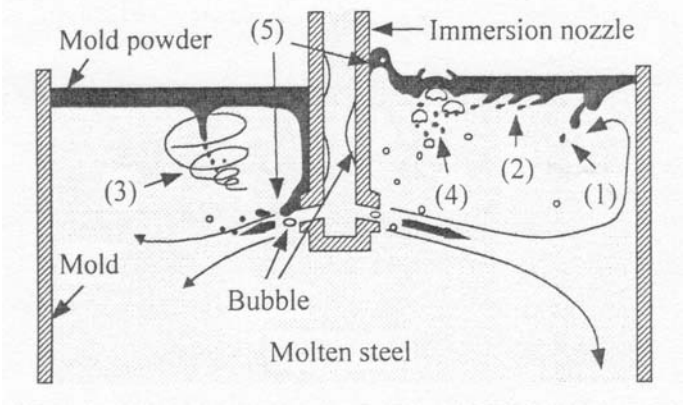


Fig.1 Mechanisms of slag entrainment in the continuous casting mold [18)]

In the current paper, fluid flow in the SEN and the mold of the slab continuous caster at Panzhihua Steel (P.R.China) is investigated using water models, numerical simulations and industrial measurements. In the water model, the top surface fluctuation, the pressure near the jet impingement point on the narrow face, and the flow patterns are measured. The effects of the submergence depth, SEN geometry, mold width, water flow rate, and gas flow rate are investigated. Three-dimensional fluid flow in the water model of the tundish, the SEN and the mold are calculated with numerical simulations, solving the continuity equation, momentum equations, turbulent energy and its dissipation rate equations [32)] using Fluent software. The trajectories of inclusions and bubbles are predicted by considering the buoyancy and drag forces acting on the bubbles and including the effect of turbulent fluctuation of the fluid flow with the Random-Walk model[32)]. In the industrial trial, the thickness of the liquid flux, inclusions in the steel, and inclusion removal to the mold flux are measured. The effect of the SEN well shape on the steel cleanliness is investigated.

## WATER MODEL EXPERIMENTS AND SIMILARITY CRITERION

The Weber-Froude similarity criterion is used to design the water model for the gas-water two phase fluid flow phenomena. The Froude number, *Fr*, is given by

$$Fr = \frac{U^2}{gL} \tag{1}$$

where $U$ is the characteristic velocity (m/s), $g$ is the gravitational acceleration rate (m/s$^2$), $L$ is the characteristic length (m). Invoking Froude similarity between a water model (w) and a steel caster (s) gives:

$$\left(\frac{U^2}{gL}\right)_{\mathrm{w}} = \left(\frac{U^2}{gL}\right)_{\mathrm{s}} \tag{2}$$

Substituting the geometry scale factor, $\lambda=L_w/L_s$, into Eq.(2) gives:

$$\frac{U_w}{U_s}=\sqrt{\lambda} \tag{3}$$

The Weber number, *We*, is given by

$$We=\frac{\rho U^2 L}{\sigma} \tag{4}$$

where $\rho$ is the liquid density, 7020kg/m$^3$ for molten steel and 998 kg/m$^3$ for water, and $\sigma$ is the surface tension, 1.6 for molten steel and 0.073N/m for water. Applying Weber similarity between a water model (w) and a steel caster (s) implies

$$\left(\frac{\rho U^2 L}{\sigma}\right)_w=\left(\frac{\rho U^2 L}{\sigma}\right)_s, \tag{5}$$

which gives

$$\left(\frac{U_w}{U_s}\right)^2=\frac{L_S}{L_w}\frac{\rho_S}{\rho_w}\frac{\sigma_w}{\sigma_S}=\frac{1}{\lambda}\frac{\rho_S}{\rho_w}\frac{\sigma_w}{\sigma_S}. \tag{6}$$

Inserting Eq.(3) into (6) yields

$$\lambda=\left(\frac{\rho_S}{\rho_w}\frac{\sigma_w}{\sigma_S}\right)^{1/2}, \tag{7}$$

which gives

$$\lambda\cong 0.6. \tag{8}$$

Hence if $\lambda$=0.6, both Froude similarity and Weber similarity can be satisfied simultaneously. The relationship between the water flow rate ($Q_w$) and the molten steel throughput ( $Q_S$) (m$^3$/hour) is

$$\frac{Q_w}{Q_s}=\frac{U_w L_w^2}{U_s L_s^2}=\lambda^{2.5}=0.279 \tag{9}$$

It should be mentioned here that even though both the Froude similarity and the Weber similarity are satisfied, the similarity between the water and the steel still need to be further investigated. Recent work has found that the multiphase fluid flow pattern in a full scale water model does not match the fluid flow pattern in the molten steel caster, although the numerical simulation can match both. [33, 34)]

A schematic of the water model experiment is shown in Figure 2. A straight-mold steel caster of a 200mm thick and 1250mm wide strand is modeled with a water model that is 1200mm in length, 120mm in thickness, and varies in width from 774.6mm at the top to 753.3mm at the bottom. A second strand width of 900mm is modeled with a top width of 557.7mm, and bottom width of 542.4mm. The example SEN configuration is also shown in Fig. 2. The $N_2$ gas, used to model the argon gas in the molten steel, is injected into the mold through a central circular hole (4mm in diameter) in the bottom of the stopper rod. Firstly the water heights in the tundish and in the mold are adjusted to be steady by adjusting the flow meter and the position of the stopper rod. The water height in the tundish is 600mm if not specified otherwise. The steady flow state is maintained for 5 minutes and then the level fluctuation, impingement pressure, and location of the lower roll center are measured three times, and the mean is recorded. The definition of the level fluctuation is the mean of the 5 largest level fluctuations during each 40s measurement. This is because large level fluctuations account more for the slag entrainment than small ones. There should be some surface flow, including level fluctuations at the meniscus, in order to prevent the meniscus from freezing, but it should not be excessive to induce slag entrainment. Level fluctuations of 6-9mm at the meniscus of continuous-cast cold-rolled coil was reported to have the fewest surface defects. [13)] This corresponds to optimal level fluctuations in the water model of 3.6-5.4mm. The level fluctuation at ¼ width should be as small as possible. The impingement pressure is the mean of the measured pressure for 40s measured near the impingement point of the narrow face, subtracting the static water pressure ($\rho_w gh$). Lower pressures might be better. The lower roll location is the distance from the top surface to the center of the lower roll. Smaller values should improve inclusion removal to the top surface. Of these parameters, the most important is the magnitude of the level fluctuations.

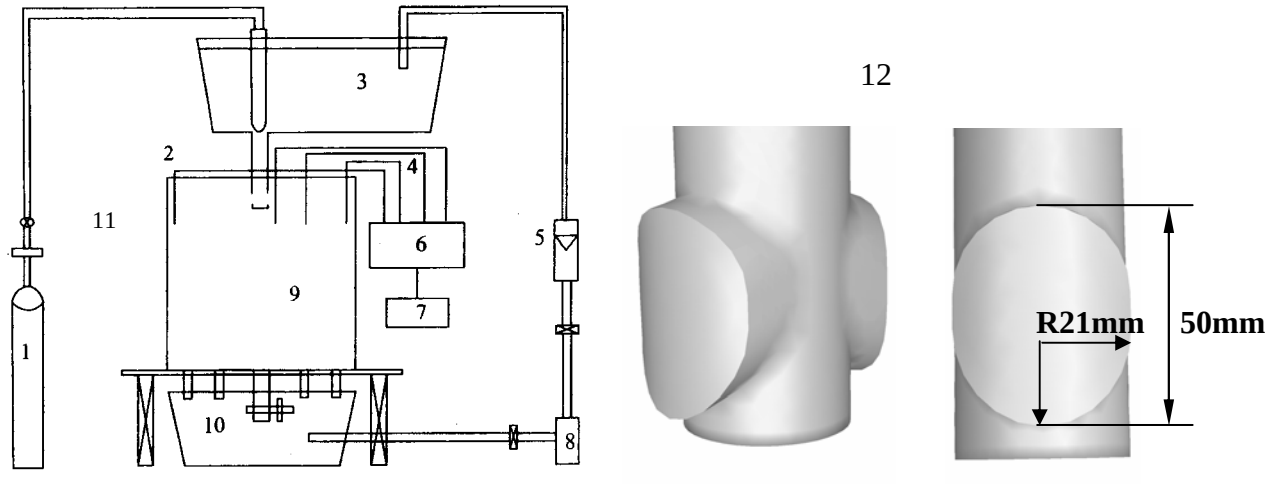


Fig.2 Schematic of the water model experiment (1: $N_2$ tank, 2: pressure measurement probe, 3: tundish, 4: level fluctuation measurement probes, 5: water flow meter, 6: Data collection system, 7: Computer, 8: pump, 9: mold, 10: water collection tank, 11: gas flow meter, 12: dimension of the SEN outports)

The parameters used in the water model experiment are shown in Table I. The effects of casting speed, SEN submergence depth, gas flow rate, SEN outport angle, inner diameter of SEN, the area ratio ψ (the area of the SEN bore to the total area of the two outports), and the bottom well shape on the level fluctuation, the impingement pressure and the location of the lower roll center are investigated. The relationship between the casting speed and the flow rate of the water and the steel is shown in Table II.

Table I Parameters used in the water model

| Casting speed (m/min) | SEN submergence depth (mm) | Gas flow rate (Nl/min) | SEN outport angle | Bore diameter of the SEN | Port to bore area ratio ψ |
|---|---|---|---|---|---|
| 1.0 | 40 | 0 | +5° | 30 mm | 0.67 |
| 1.2 | 70 | 4.58 | 0° | 35 mm | 0.58 |
| 1.4 | 100 | 9.16 | -5° | 40 mm | 0.50 |
| 1.6 | 130 | 13.74 | -15° | 45 mm | 0.44 |
| 1.8 | 160 | 18.32 | -25° | 50 mm | 0.40 |

Table II Relationship between the flow rate and the casting speed

| | Casting speed (m/min) | 1.0 | 1.2 | 1.4 | 1.6 | 1.8 |
|---|---|---|---|---|---|---|
| 200mm×900mm slab | Steel throughput ($m^3$/hour) | 11.898 | 14.28 | 16.656 | 19.038 | 21.414 |
| | Water throughput ($m^3$/hour) | 3.318 | 3.984 | 4.65 | 5.31 | 5.976 |
| 200mm×1250mm slab | Steel throughput ($m^3$/hour) | 13.218 | 16.524 | 19.83 | 23.136 | 26.442 |
| | Water throughput ($m^3$/hour) | 3.69 | 4.716 | 5.532 | 6.582 | 7.38 |

## MULTIPHASE FLUID FLOW PATTERN IN THE SEN

There are three kinds of fluid flow pattern in the SEN, as shown in Figure 3: bubbly flow (Fig.3a), annular flow (Fig.3b) and critical flow between these two (Fig.3c). For the bubbly flow pattern, the water and the gas are well mixed, and the jets at the two outports are relatively uniform and symmetrical. The turbulence in the SEN is very strong, so both the liquid phase and the gas phase have large energy losses, leading to a small jet energy and low impingement pressure at the narrow face. In addition, the strong interaction between the gas and the liquid in the SEN tends to dislodge any inclusions just attached to the SEN walls, which lowers the tendency for clogging. For the annular flow pattern, the liquid annularly enters the SEN and then flows down along the walls, as it periodically changes its position. The liquid flow separates from the gas, which forms large pockets just below the stopper. The energy loss is small, so the impingement pressure to the narrow face is high. The flow is unstable, so the jets from the two outports tend to be asymmetrical. A given outport, may emit more gas and less water, as the large gas regions escape and move intermittently along the outer walls of SEN to the top surface, where they rupture. This creates large level fluctuations and even generates foams near the SEN.[28] At the other outport, there may be more water and less gas, which gives the jet has a large momentum and speed, leading to high impingement pressure on the narrow face, and big level fluctuations at the meniscus. For the critical flow pattern, part of the inside of the SEN is bubbly flow, and the rest is annular flow. A tiny change of the water height in the tundish, casting speed, or gas flow rate can switch this critical flow to annular flow or to bubbly flow. If the flow regime suddenly switches to annular flow, the resistance to flow increases, which causes the water height in the tundish to increase abruptly, and the level in the mold to decrease abruptly. Water

may even overflow the tundish. If the flow regime suddenly switches to bubbly flow, the resistance to flow decreases, which causes the water height in the tundish to decrease abruptly, and the level in the mold to increase abruptly. Water may even overflow the mold.

(a) bubbly flow (b) annular flow (c) critical flow

Fig.3 The multiphase fluid flow pattern in the SEN with 45mm bore diameter

The flow pattern in the SEN with a fixed bore diameter is mainly affected by the liquid flow rate, the gas flow rate, and the liquid height in the tundish, as shown in Figure 4. When the casting speed is increased, the gas flow rate required to obtain bubbly flow is also increased. In order to achieve the bubbly flow pattern in the SEN, the operation conditions should lie below the curves in Fig4. For example, if the water throughput is 6m$^3$/hour, and the liquid height in the tundish is 600mm, the gas flow rate should be smaller than 19.5 Nl/min to achieve bubbly flow. Increasing liquid height in the tundish needs a greater gas flow rate in order to achieve bubbly flow in the SEN, with other conditions kept constant.

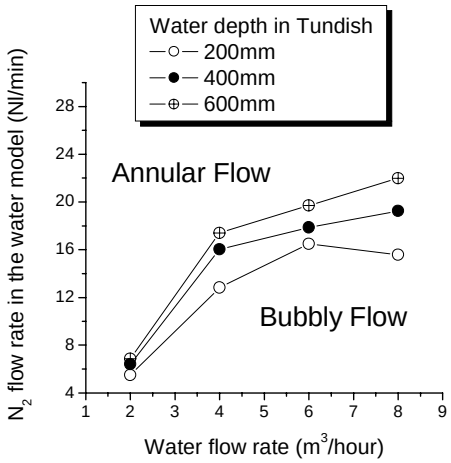


Fig.4 The conditions to achieve annular flow or the bubbly flow in a 45 mm SEN (water model)

In the real steel caster, the bubbly flow pattern in the SEN is desired to prevent unstable and asymmetrical flow in the mold. Fig.4 can be converted into the steel-argon system using the similarity criterion (Eq.(9)) as follows:

$$Q_w = 0.279 Q_S = 0.279 \times \left( S \cdot V_C \cdot 60 \cdot \frac{7800}{7020} \right)$$

where $S$ is the cross-section area of the strand (mm$^2$), $V_C$ is the steel casting speed (m/min), and 7800/7200 is the ratio of the solid steel density to the liquid steel density. So for the 200mm×900mm strand,

$$V_C = 0.298\ Q_w, \tag{10}$$

and for the 200mm×1250mm strand,

$$V_C = 0.214\ Q_w. \tag{11}$$

The argon flow rate to use in the steel continuous casting can be derived from the modified Froude number defined as:

$$\mathrm{Fr}' = \frac{\rho_g V_g^2}{(\rho_l - \rho_g) g L} \tag{12}$$

where $\rho_g$ and $\rho_l$ are the density of the gas and the liquid (kg/m$^3$), and $V_g$ is the gas velocity (m/s). Here $\rho_w$=998 kg/m$^3$, $\rho_s$=7020 kg/m$^3$, $\rho_{Ar}$=1.783 kg/m$^3$, $\rho_{N2}$=1.251 kg/m$^3$. The gas flow rate $Q_g=V_g \cdot 1/4\pi D_n^2$, where $D_n$ the diameter of the hole in the stopper rod through which the gas enters the SEN. In the water model, $D_{n,w}$=0.004m, and in the steel caster $D_{n,s}$=0.005m. This criterion gives

$$\frac{\rho_{N_2} V_{N_2}^2}{(\rho_w - \rho_{N_2}) \cdot g \cdot L_w} = \frac{\rho_{Ar} V_{Ar}^2}{(\rho_S - \rho_{Ar}) \cdot g \cdot L_S}, \tag{13}$$

which yields the following expression at standard pressure (1atm) and 1550$^o$C

$$Q_{Ar}=2.885 Q_{N2} \tag{14}$$

Considering the six-fold volumetric of gas injected and heated to steel temperature, the argon gas flow at the standard temperature (0$^o$C) should be

$$Q_{Ar}=0.420 Q_{N2} \tag{15}$$

By Eq.(10), (11) and (15), Fig.4 can be redrawn into Figure 5 for the steel continuous casting process. For the continuous casting of the 200mm×1250mm steel slab with 1.1m/min casting speed and 1000mm steel height in the tundish, the argon gas flow rate should be below 6.5 Nl/min to get the bubbly flow pattern in the SEN. However, in the real continuous casting process at Panzhihua steel, the gas flow rate is 10-20Nl/min, under which the flow in the SEN is the annular flow pattern, inducing the biased flow pattern in the mold, serious level fluctuation and slag entrainment. In the continuous caster, the periodic "jumping of the fish"— open eye of the molten steel induced by the serious level fluctuation at the ¼ width of the mold is observed. After using the optimized SEN configuration and with suitable gas flow rate, this phenomenon of "jumping of the fish" is finally diminished. At some special cases such as the ladle change period, the steel height in the tundish and the casting speed decrease, the gas flow rate should be much smaller in order to achieve the bubbly flow in the SEN.

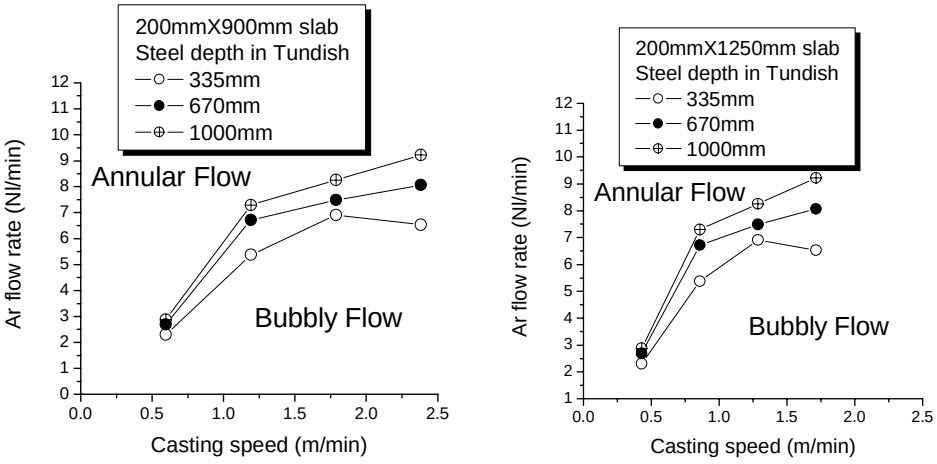


Fig.5 The conditions to change annular flow to bubbly flow in a 75 mm SEN (liquid steel)

## MULTIPHASE FLUID FLOW PATTERN IN THE MOLD

There are two main flow patterns in the mold: single roll and double roll. The single roll flow pattern is more likely with high gas injection, small SEN submergence depth and small casting speed. The double roll flow pattern is manly induced by large casting speed, large SEN submergence depth, and small gas flow rate. The single phase fluid flow pattern is usually double roll, and its typical simulation is shown in Figure 6. There is little backflow at the outports of the SEN. The jet impinges the narrow face, where part of the flow moves upwards along the narrow face to form the upper roll, and another part flows downwards to generate the lower roll.

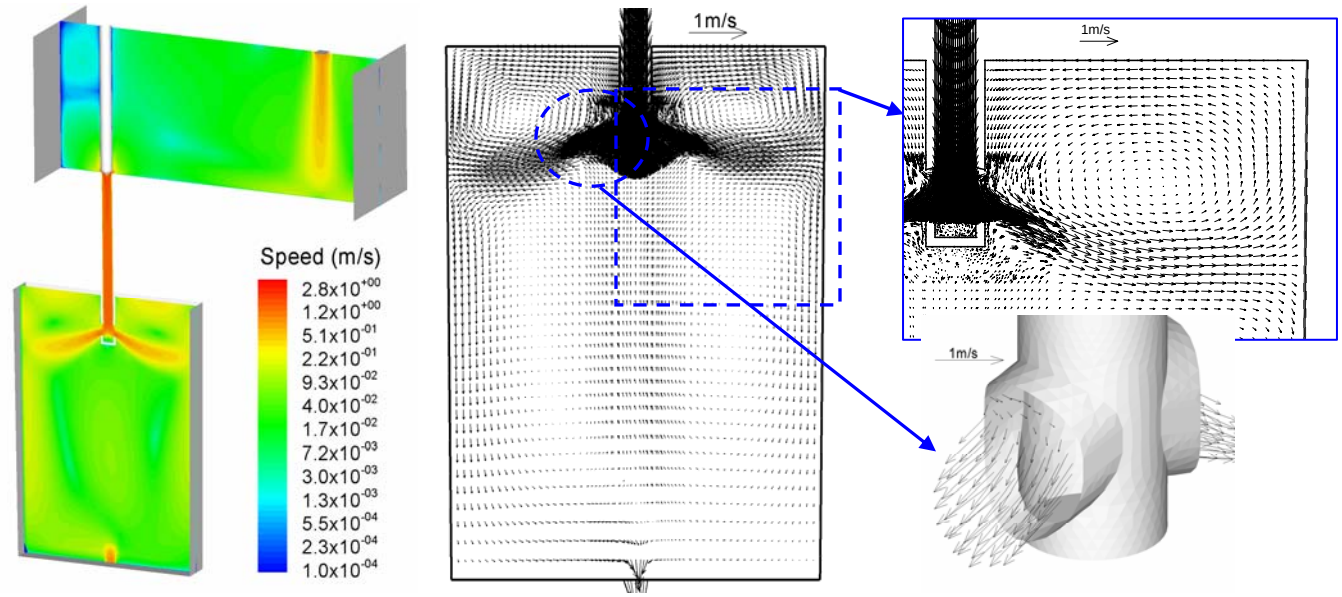


Fig.6 Calculated single phase fluid flow in the tundish, the SEN and the mold (water model of the 200mm×1250 mold, casting speed: 1.4 m/min, tundish inlet velocity: 0.731 m/s, inlet turbulent energy: 0.004 $m^2/s^2$, and its dissipation rate: 0.03 $m^2/s^3$, SEN bore diameter: 45mm, outport angle: down 15°, Submergence depth of the SEN: 130mm, water height in the tundish: 600mm, tundish length: 1400mm, tundish thickness: 400mm)

Typical calculated trajectories of 10 bubbles with the size of 1mm (a,b) and 5mm (c,d) in the water mold of Fig.6 are shown in Figure 7. Very rarely, a few large bubbles may penetrate deep and be entrapped through the bottom outlet. More of the 1mm bubbles enter the outlet at the bottom of the mold than the 5mm bubbles. Due to the turbulent fluctuation, the motion of the bubbles in the mold is very chaotic, varying from symmetrical to asymmetrical, which corresponds with transient biased flow in the mold. At optimal levels, bubbles injected into the nozzle are helpful by reducing nozzle clogging, changing the fluid flow pattern with their buoyancy effect favoring inclusion removal, and decreasing the impingement pressure at the narrow face, and capturing inclusions as they flow in the liquid [28, 35-37]. However, if the casting speed is too large or the gas flow rate is too high, some bubbles (especially small ones) can entrap solid oxide particles and turn to be captured by the solidifying shell, eventually leading to surface slivers or internal defects. [28] Bubbles may also be entrapped at the meniscus, especially if large oscillation hooks or large level fluctuations occur. If the gas flow rate is too large for the casting speed, large bubbles can exit the port tops, move up along the outer SEN walls, and emulsify the slag at the top surface near the SEN. The gas flow rate should be adjusted according to the casting speed and other flow parameters, as discussed in detail elsewhere. [29) 38-40)]

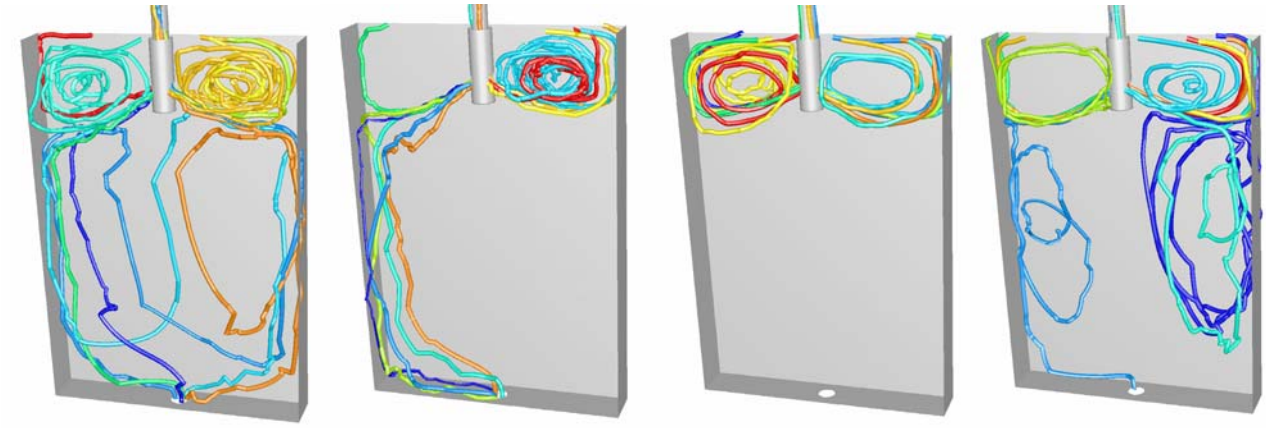

(a) (b) (c) (d)

Fig.7 Typical random walk trajectories of 10 bubbles with the size of 1mm (a,b) and 5mm (c,d) in the water mold of Fig.6

Increasing gas injection encourages a single roll flow pattern, which tends to increase top surface fluctuations. Figure 8 shows examples of the flow pattern progressing from single roll to double roll in the water model. In the single roll flow pattern (a and b), the level height near the SEN is very large, whereas with the strong double flow pattern (c), the level height near the narrow face is large. Decreasing casting speed with the same gas injection also encourages the single roll flow pattern, as shown in Figure 9. Table III

summarizes the resulting single or double roll flow patterns obtained in the water model. Low gas flow tends to double-roll flow pattern, while a high argon flow rate induces single-roll flow. To maintain a stable double-roll flow pattern, which is often optimal, the argon should be kept safely below a critical level. [41-43] Excessive argon injection may generate transient variations of the jets entering the mold, introduce asymmetry in the mold cavity, [44] and increase surface turbulence.

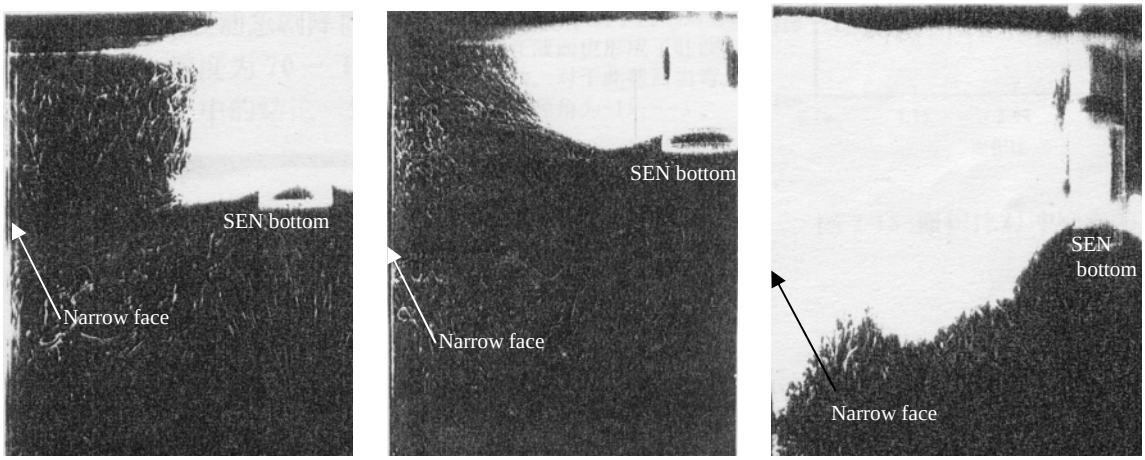


(a) (b) (c)

| | Casting speed | Submergence depth of SEN | Gas flow rate | Outport angle of the SEN | Bore size of the SEN | Port to bore area ratio ψ |
|---|---|---|---|---|---|---|
| (a) | 1.2 m/min | 100 mm | 4.6 Nl/min | -15° | 50 mm | 0.67 |
| (b) | 1.4 m/min | 40 mm | 13.7 Nl/min | -5° | 50 mm | 0.58 |
| (c) | 1.8 m/min | 130 mm | 18.3 Nl/min | -5° | 35 mm | 0.67 |

Fig.8 Fluid flow pattern in the 200mm×1250mm mold progressing from the single roll to the double roll

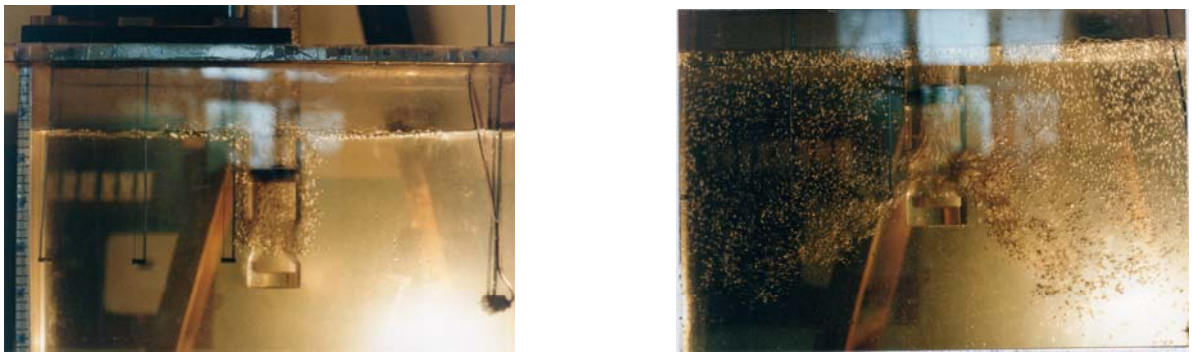

(a) (b)

Fig. 9 Two phase fluid flow pattern in the water model of the 200mm×1250mm steel slab (bore diameter of the SEN: 45mm, gas flow rate: 5.344 Nl/min, submergence depth of the SEN: 100mm, water flow rate: (a) 2.0 $m^3$/hour, (b) 6.6 $m^3$/hour

Table III Fluid flow pattern in the water model the mold

| Strand size | Casting speed | Gas flow rate | SEN | | | | Flow pattern |
|---|---|---|---|---|---|---|---|
| | | | Submergence depth | Outport angle | Bore size | Area ratio ψ | |
| 200mm ×900mm | 1.0m/min | 4.6 Nl/min | 70 mm | 0° | 35 mm | 0.58 | Double roll |
| | 1.2m/min | 4.6 Nl/min | 100 mm | -15° | 50 mm | 0.67 | Single roll |
| | 1.4m/min | 13.7Nl/min | 40 mm | -5° | 50 mm | 0.58 | Single roll |
| | 1.8m/min | 9.2 Nl/min | 70 mm | +5° | 50 mm | 0.44 | Double roll |
| | 1.8m/min | 13.7 Nl/min | 100 mm | 0° | 30 mm | 0.40 | Double roll |
| | 1.8m/min | 18.3 Nl/min | 130 mm | -5° | 35 mm | 0.67 | Double roll |
| 200mm ×1250mm | 0.8m/min | 0 Nl/min | 40 mm | +5° | 30 mm | 0.67 | Double roll |
| | 0.8m/min | 9.2 Nl/min | 100 mm | -5° | 40 mm | 0.50 | Single roll |
| | 1.0m/min | 0 Nl/min | 70 mm | -5° | 45 mm | 0.40 | Double roll |
| | 1.0m/min | 4.6 Nl/min | 100 mm | -15° | 50 mm | 0.67 | Single roll |
| | 1.2m/min | 18.3 Nl/min | 40 mm | 0° | 40 mm | 0.44 | Single roll |
| | 1.2m/min | 9.2 Nl/min | 160 mm | 0° | 45 mm | 0.67 | Double roll |
| | 1.2m/min | 13.7 Nl/min | 40 mm | -5° | 50 mm | 0.58 | Single roll |

It was observed that inclusion entrapment varies from side to side, which suggests a link with asymmetrical variations in the transient flow structure in the mold. The associated asymmetrical surface velocities induce vortices at the top surface. In the water model, the vortex location was observed to move periodically with time. This asymmetrical flow could be induced by the following causes:

1) Operational Conditions
   - Off-center of stopper rod, and off center gas injection from the stopper rod;
   - Off center location of the SEN in the mold;
   - Uneven bottom of the SEN;
   - Asymmetrical design of the two outports including the port diameter and port angle;
   - Non-uniform and asymmetrical gas injection from the up nozzle, slide gate, or porous brick of the SEN;
   - Changes in casting speed or gas flow rate during the start or end of pouring and during ladle changes;
2) Fluid flow in the SEN and in the mold
   - Asymmetrical inflow at the bottom well of the tundish;
   - Chaotic nature of turbulence of the fluid flow in the mold [8, 45];
   - Annular flow in the SEN (Fig.3);
   - Transient flow oscillations induced by the gas injection;
   - Transient biased random motion of bubbles (Fig.7).

It is especially important to keep nearly constant liquid steel level in the mold, constant powder feeding rate, constant casting speed, constant gas injection fraction, [40] constant slide gate opening, and fixed nozzle position (alignment and submergence). Figure 10 shows the low frequency oscillations (b) after filtering out the high frequency fluctuation (c) from (a). The high frequency fluctuation (Fig.10c) is mainly generated by the turbulence. The low frequency flow oscillation stems from the asymmetrical flow in the mold. The magnitude of the low and high frequency components is similar, around 10mm. However, the longer duration of the low frequency oscillation, may make this component worse for causing quality problems.

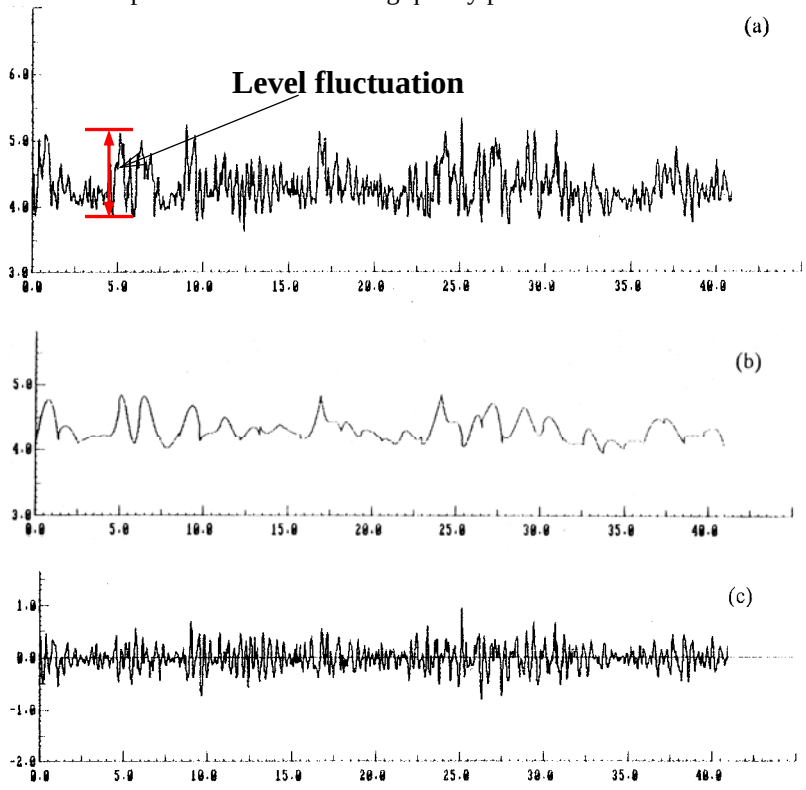


Fig.10 Example measured level fluctuation signal (a) split into low frequency (b) and high frequency (c) components

## OPTIMIZATION OF FLUID FLOW IN THE SEN AND IN THE MOLD

Level fluctuations are mainly induced by the jet impingement and upwards flow along the narrow face, rupture of bubbles at the top of the liquid, the single roll flow pattern in the mold, the transient biased fluid flow in the mold especially with gas injection, and the turbulence itself. Level fluctuations at the meniscus increase with increasing gas flow rate , (Figure 11). When the casting speed is low, the gas mainly exits the top surface near the SEN, as shown in Fig.9a. So level fluctuations are worse near the SEN. With high casting speed, the bubbles tend to exit closer to the narrow face, where level fluctuations become larger. Under the same conditions, the smaller width slab has a larger level fluctuation. This is because the turbulent energy is more easily dissipated in the larger slab.

For the same conditions, the meniscus region generally has smaller level fluctuations than the interior. To obtain 3.6-5.4mm level fluctuations at the narrow face meniscus, the gas flow rate for the 1250mm width slab should be 5.3.-6.9 Nl/min, and for the 900mm width slab, the gas flow rate should be smaller than 4.6-7.6 Nl/min.

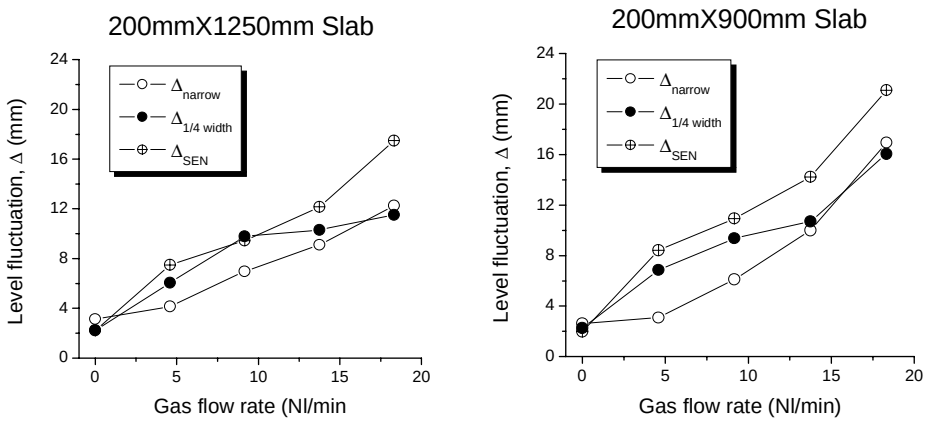


Fig. 11 Level fluctuations with different gas flow rates

Past work has found that larger casting speed tends to induce larger level fluctuations at the meniscus. For the configurations studied in this work, however, casting speed has little effect on the level fluctuations (Figure 12). This is likely due to compensating changes in the flow pattern. For example, increasing speed tends to switch from a single to a double roll flow pattern (decreasing surface velocities). This may offset the general increase in surface velocity caused by the higher speed. Moreover, flow stability and transient oscillation, which is most responsible for level fluctuations, is not directly related to speed when gas is present. .

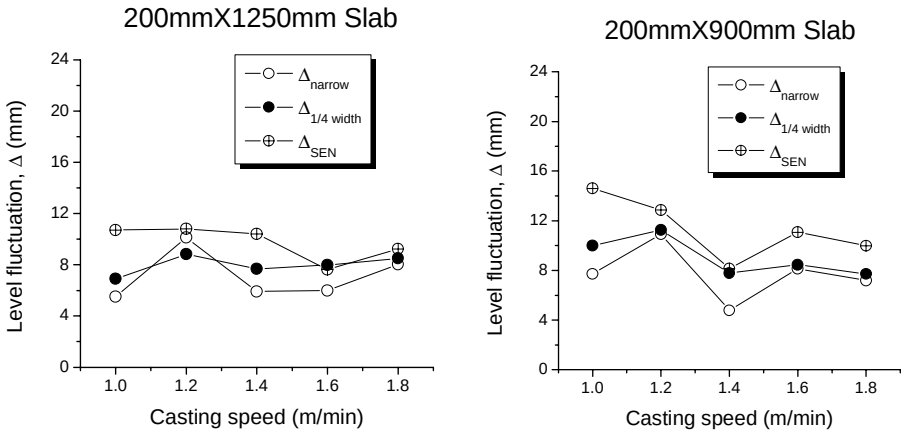


Fig. 12 Effect of casting speed on the level fluctuations

Level fluctuations at the meniscus decrease with increasing submergence depth up to about 70 mm, and then switches to increasing with further increasing the submergence depth above 100mm (figure 13). The reason for this small effect is related to the tendency to switch from single to double-roll flow pattern with increasing submergence depth. The best submergence depth is around 70-100mm, with 5.1mm level fluctuation at meniscus for the 1250mm width, and 5.7mm for the 900mm width.

Figure 14 shows that the SEN outport angle should be downwards 5-15$^{o}$. If the outport angle is outside of this range, level fluctuations increase. Increasing angle tends to generate the single roll flow pattern, which has larger level fluctuations. Too large a downward angle may generate flow pattern asymmetry, with corresponding large level fluctuations.

As shown in Figure 15, the level fluctuations decrease with increasing bore diameter of the SEN. This is likely due to decreasing the size of the channel between the SEN outer bore and the mold walls, which lowers surface velocity there. This prevents communication between the two sides of the mold, which tends to discourage flow asymmetry and the associated level fluctuations. The optimal inner diameter of the SEN is 45mm for both the 900mm and 1250mm widths. With this bore size, the level fluctuations at the meniscus are 7.27mm for the 900mm width, and 5.32mm for the 1250mm width.

Figure 16 shows that level fluctuations decrease slightly with increasing the port-to-bore area ratio $\psi$. This is due to lowering the exit velocity. However, if the area ratio is too big, it is possible to generate asymmetrical flow.

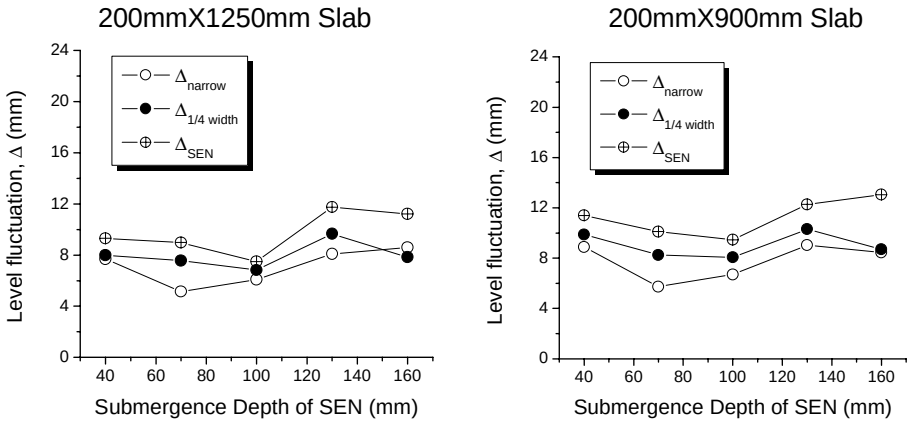


Fig.13 Effect of submergence depth on the level fluctuation in the mold

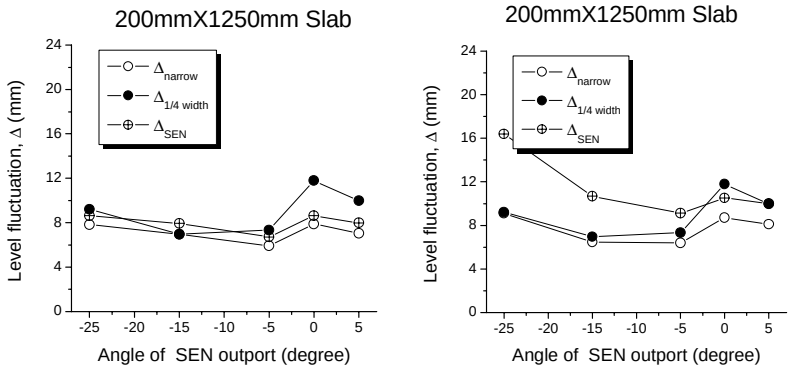


Fig.14 Effect of SEN outport angle on the level fluctuation in the mold

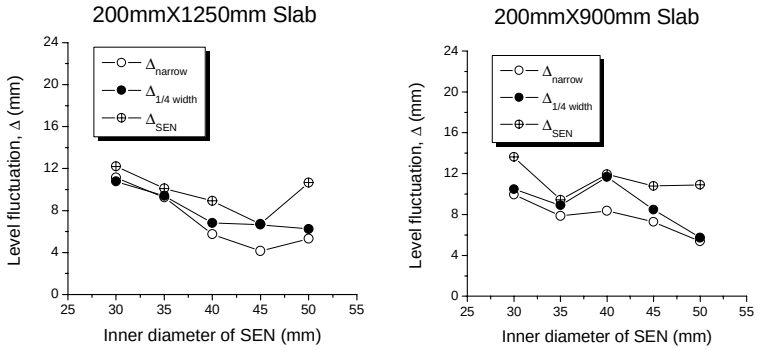


Fig.15 Effect of inner bore diameter of SEN on level fluctuations in the mold

Figure 17 shows effects of some parameters on the impingement pressure to the narrow face. For the 900mm width, the impingement pressure increases with increasing casting speed and decreasing inner diameter of the SEN. The impingement pressure is smallest for the 900mm width if the gas flow rate is 9.2Nl/min, the outport angle is downwards 15°, and the submergence depth is 100mm. If the area ratio is smaller than 0.57, the impingement pressure decreases with increasing area ratio. For the same conditions, the impingement pressure for the 1250mm width is smaller than for the 900mm width. For the 1250mm width, the impingement pressure is independent of the submergence depth and the bore diameter of the SEN. Figure 18 shows the effects of process parameters on the depth of the center of the lower recirculation roll. This point becomes deeper with increasing casting speed, decreasing gas flow rate, decreasing submergence depth, or decreasing SEN bore diameter.

All Figs 11-18 naturally indicate that the level fluctuations at the meniscus near the narrow face are smaller than those in the interior (centerline) at the ¼ width or near the SEN. They also indicate that level fluctuations for the 900mm width are larger than for the 1250mm width. The parameters chosen as optimal are listed in Table IV. A common SEN configuration is chosen for both slab widths: 45mm inner diameter, downwards 15°, and 0.45 area ratio.

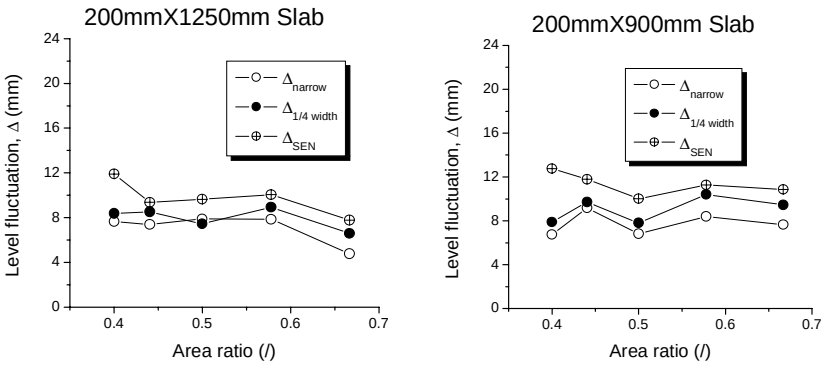


Fig.16 Effect of port-to-bore area ratio ψ on mold level fluctuations

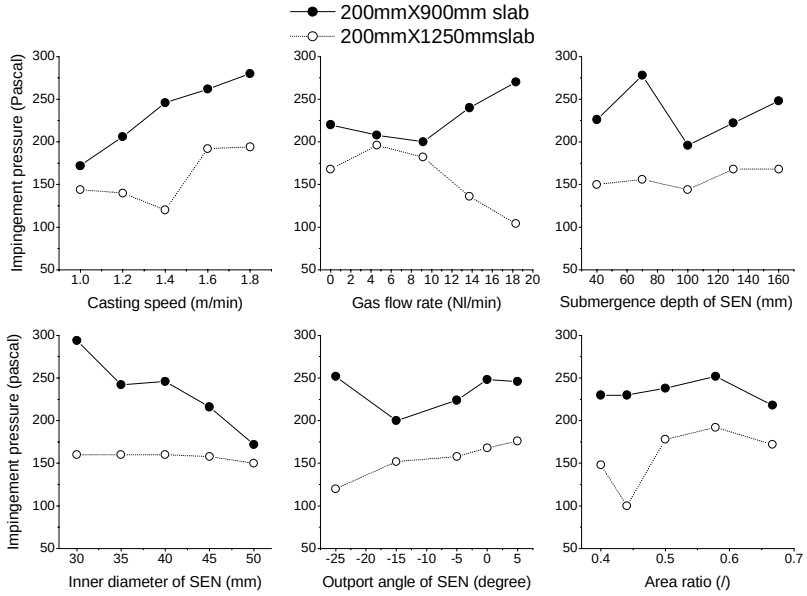


Fig.17 Factors affecting the impingement pressure

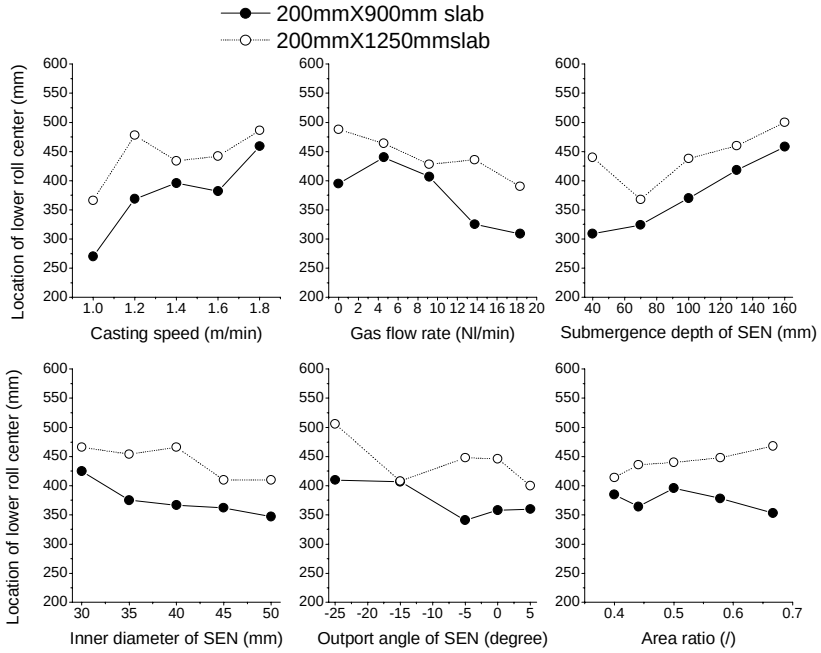


Fig.18 Factors affecting the depth of the lower roll center

Table IV Optimized configuration and parameters for SEN and continuous casting

| Strand section size ($mm^2$) | SEN configuration | | | | Casting speed | Gas flow rate |
|---|---|---|---|---|---|---|
| | Bore diameter | Outport angle | Area ratio | Submergence depth | | |
| 200×900 | 47mm | -15°— -5° | 0.476 | 85-95mm | 1.4-1.5 m/min | 4.58 Nl/min |
| 200×1250 | 43mm | -15°— -5° | 0.44 | 75-95mm | 1.2-1.3 m/min | 5.34-6.87 Nl/min |

## EFFECT OF SEN BOTTOM WELL ON THE FLUID FLOW IN THE MOLD

Two kinds of well shape of the SEN are investigated: pointed bottom SEN and recess well SEN. Water model experiments with the 200mm×1250mm mold are performed with these two bottom shapes for the chosen optimal SEN configuration with 4.6 Nl/min gas flow rate and 90mm submergence depth. The measured level fluctuation, the impingement depth and the location of the lower roll center are shown in Figure 19. For the pointed bottom SEN, the level fluctuation at the meniscus is too small, which may not provide good heat transfer at the meniscus and freeze the liquid slag. Also, the pointed bottom SEN has larger level fluctuations near the SEN than the recess bottom SEN, owing to being prone to flow asymmetry. It also has larger impingement pressure, and greater impingement depth, which is not good for the inclusion removal in the mold.

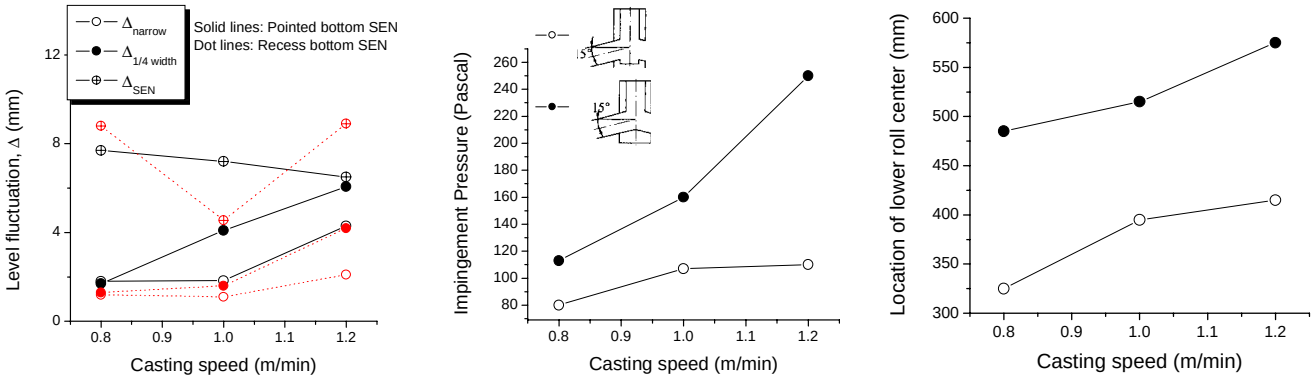


Fig.19 Measured level fluctuation, impingement pressure and the location of the lower roll center with different SEN bottom shape for the water mode of the 200mm×1250mm steel mold

## INDUSTRIAL MEASUREMENT OF STEEL CLEANLINESS WITH DIFFERENT SEN BOTTOM SHAPES

Industrial trials were performed for a 3-heat sequence (240 tonne total) cast with a slab size of 200mm×1250mm, and casting speed of 1.0-1.2m/min. To trace the origin of inclusions caused by mold slag entrainment, $La_2O_3$ is added to the mold flux before casting. The caster has two strands: strand 1 is with the recess well SEN, and strand 2 is with pointed-bottom SEN. The thickness of the liquid slag is measured at 10mm from the narrow face, at the ¼ width centerline, and 10mm from the SEN. Liquid flux samples are taken to analyze the change in $Al_2O_3$ content during continuous casting. Steel samples are taken from the mold at the ¼ width and 100 mm below the surface of the molten steel to analyze the total oxygen and the nitrogen in the steel. Slab samples are taken to observe micro inclusions with an optical microscope and large inclusions (>50μm) with Slime tests [46]. Table V shows the micro inclusions found by the microscope observations. Strand 2 (pointed-bottom SEN) has lower cleanliness.

Table V Area percentage (%) of inclusions by the microscope obervation

| Samples | 1 | 2 | 3 | 4 | 5 | Mean |
|---|---|---|---|---|---|---|
| Strand 1 | 0.1789 | 0.1994 | 0.0890 | 0.0508 | 0.0481 | 0.11324 |
| Strand 2 | 0.1991 | 0.1906 | 0.1083 | 0.0764 | 0.0786 | 0.1306 |

The measured thickness of the liquid flux layer is shown in Table VI. The liquid flux at the narrow-face meniscus is 1-3mm thicker than that at ¼ width and near the SEN. The recess-well SEN generates 3mm more liquid flux thickness than the pointed-bottom SEN. POSCO reported that for the low carbon Al-killed steel, if the casting speed is 1.0-1.6m/min, the best thickness of the liquid slag layer is 10-15mm. [47] In the current investigation, Strand 2 (pointed-bottom SEN) had insufficient slag layer thickness. This could disrupt meniscus solidification, leading to deep hooks, which can capture bubbles and inclusions. This might explain the lower cleanliness observed for the pointed-bottom SEN.

Inclusion absorption from the molten steel into the liquid flux on top of the mold has 2 components: 1) increasing the $Al_2O_3$ content from the mold powder composition (2.84% $Al_2O_3$) to the measured alumina concentration at steady state and 2) maintaining that value as flux is consumed. Based on the measured liquid flux thickness (Table VI) and assuming a liquid slag density of 3500 $kg/m^3$, the mass of the liquid slag layer is 10.59kg (strand 1) and 8.46kg (strand 2). This corresponds to 0.47kg of $Al_2O_3$ from the steel (strand 1)

and 0.44kg (strand 2), as given in Table VII. Next, based on the mold flux consumption rate of 0.5 kg/tonne, and total of 120 tonnes of steel cast per strand during the sequence, the total liquid slag consumed from the top surface is 60kg per strand . Multiplying by the percent $Al_2O_3$ increase in the liquid slag layer in Table VII gives a consumed mass of 2.63 kg (strand 1), and 3.15 kg (strand 2). Dividing the total increase (3.10kg strand 1 and 3.59kg strand 2) over the entire heat (120 tonnes per strand) and converting from alumina (102g/mol) to oxygen (48g/mol) gives 12.2ppm total oxygen removed from the steel (strand 1) and 14.7ppm (strand 2).

Table VI Measured thickness of liquid slag layer on the top of the mold (mm)

| | Near the meniscus | ¼ width | Near the SEN | Mean thickness |
|---|---|---|---|---|
| Strand 1 | 14 | 13 | 12 | 12.9 |
| | 14 | 11 | 10 | |
| | 15 | 13 | 13 | |
| Strand 2 | 11 | 10 | 10 | 10.3 |

Table VII Measured $Al_2O_3$ fraction in the liquid flux of the mold and estimated total oxygen removal in the steel by SEN and the mold (initial $Al_2O_3$ content in the flux: 2.84%)

| | Liquid slag on the top of the mold | $Al_2O_3$ fraction in the liquid slag (%) | | | | $\Delta Al_2O_3$ in liquid slag | | Rough estimation of T.O. removal to the mold slag (ppm) |
|---|---|---|---|---|---|---|---|---|
| | | Heat 1 | Heat 2 | Heat 3 | Mean | % | kg | |
| Strand 1 | 10.59kg | 9.08 | 6.89 | 5.71 | 7.23 | 4.39 | 0.465 | 12.2ppm |
| Strand 2 | 8.46kg | 7.73 | 7.35 | 9.19 | 8.09 | 5.25 | 0.444 | 14.7ppm |

The mean of the total oxygen of the molten steel in the mold with recess bottom SEN is around 59±35ppm (Figure 20). It is assumed that the total oxygen in the tundish entering both strands has similar total oxygen values. Then, inclusion removal is 20.7% from strand 1, and 23.9% from strand 2. This inclusion removal fraction by the mold slag matches the measured and simulated fractions of inclusions removed in the mold of a different 250mm×1300mm caster using a different measurement method. [48] Moreover, in the slab of strand 1, the total oxygen is estimated to be 59×(100%-20.7%)=46.8±28ppm, which matches well with the measurement of 47±20ppm total oxygen in a slab from this strand. The greater inclusion removal fraction from strand 2 might be due to statistical variations, or it might indicate that mold slag entrainment is an important source of inclusions (not accounted for in this rough calculation) that is a more serious problem for the pointed bottom nozzle.

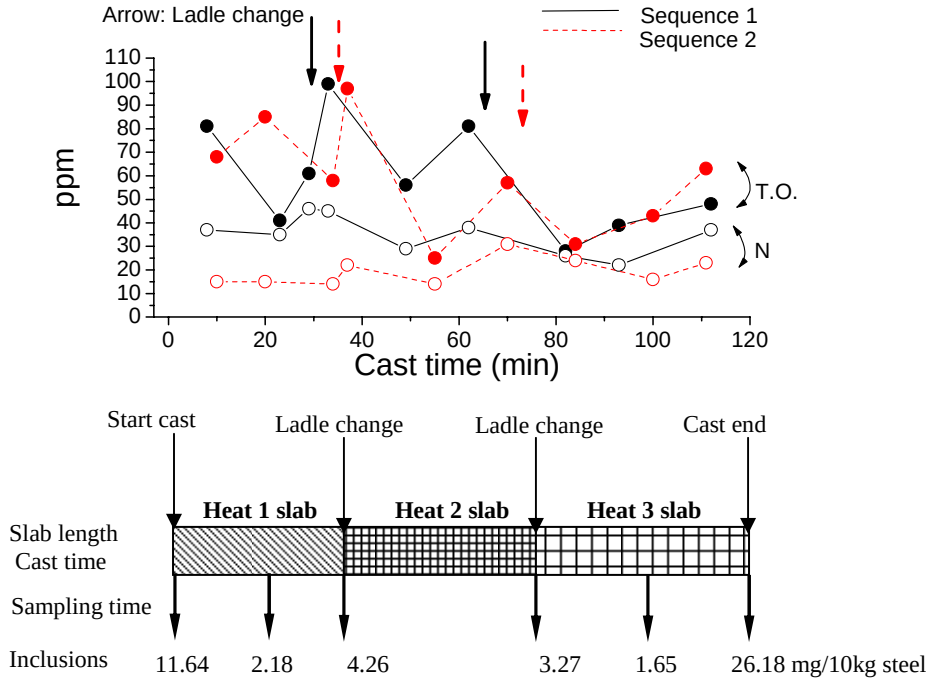


Fig.20 Total oxygen and nitrogen content in the mold (up figure) and >50μm inclusions in the slab by Slime test (lower figure)

The steel cleanliness is complicated greatly by the variations that occur during startup, ladle change periods, and end of casting. This is investigated for the two SEN bottom shapes by measuring the total oxygen and nitrogen in the molten steel in the mold as a function of casting time and the amount of large inclusions in the slab extracted by the Slime method. The results, given in Fig. 20, show that there is an abrupt increase in inclusions at the time of each ladle change. This may be induced by reoxidation from air absorption, slag entrainment in the tundish (due to emulsification during ladle opening or due to the lower tundish level), asymmetrical fluid flow from

annular flow in the SEN induced by the low casting speed and other reasons. Furthermore, he starting and ending of casting have more inclusions than any other period. This is when the above air absorption and slag entrainment phenomena are the most extreme. The period of the ladle change (3.3-4.3mg inclusions 10kg steel) has twice the cleanliness problem of steady state pouring (1.6-2.2 mg inclusions per 10 kg steel).. Figure 21 shows the typical large inclusions in the slab, many of which contain $La_2O_3$ tracer (Table VIII), indicating mold slag. This demonstrates that mold slag entrainment is a serious problem during continuous casting. Further efforts should focus on optimizing the mold flow pattern to decrease mold slag entrainment.

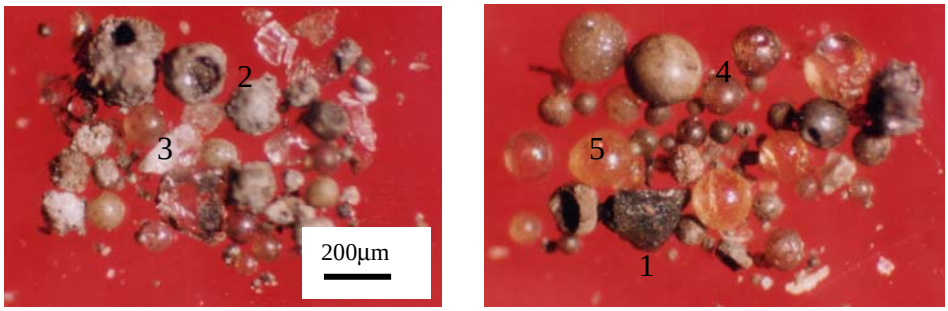


Fig.21 Typical large inclusions in the slab extracted by the Slime method

Table VIII Composition of typical large inclusions in the slab stemming from the mold slag entrainment

| | |
|---|---|
| 1 | $Al_2O_3$ 40.11%, CaO 33.70%, $SiO_2$ 20.02%, **$Na_2O$ 4.62%**, **$La_2O_3$ 1.56%** |
| 2 | $Al_2O_3$ 65.30%, FeO 26.49%, CaO 2.1%, $SiO_2$ 2.84%, MnO 0.85%, $TiO_2$ 0.30%, BaO 0.13%, **$La_2O_3$ 0.065%** |
| 3 | $Al_2O_3$ 76.49%, FeO 13.82%, CaO 3.2%, $SiO_2$ 3.47%, MnO 0.28%, $TiO_2$ 0.06%, BaO 0.25%, $La_2O_3$ 0.13% |
| 4 | $Al_2O_3$ 2.86%, FeO 6.79%, CaO 0.18%, $SiO_2$ 87.26%, MnO 0.15%, $TiO_2$ 0.26%, BaO 0.94%, **$La_2O_3$ 0.49%, $Na_2O$ 0.40%, $K_2O$ 1.12%** |
| 5 | $Al_2O_3$ 2.38%, FeO 1.23%, CaO 4.47%, $SiO_2$ 80.07%, MnO 0.03%, $TiO_2$ 0.13%, BaO 0.55%, **$La_2O_3$ 0.65%, $Na_2O$ 9.27%, $K_2O$ 1.96%** |

## SUMMARY

In the current paper, multiphase fluid flow and particle motion in the SEN and the mold of the slab continuous caster at Panzhihua Steel is investigated using water models, numerical simulations and industrial measurements. In a 0.6-scale water model, designed according to the Weber-Froude similarity criterion, the top surface level fluctuations, the jet impingement pressure, and the flow pattern in the SEN and the mold are measured. The effects of SEN geometry, submergence depth, mold width, casting speed, and gas flow rate are investigated. Three kinds of fluid flow pattern are observed in the SEN: bubbly flow, annular flow, and an intermediate critical flow structure. The annular flow structure induces detrimental asymmetrical flow in the mold. Moreover, its higher resistance to flow makes switching between flow structures prone to level fluctuations, which is even more detrimental. The SEN flow structure depends on the liquid flow rate, the gas flow rate, and the liquid height in the tundish. The gas flow rate should be adjusted with changes in the casting speed in order to maintain stable bubbly flow. Two main flow patterns are observed in the mold: single roll and double roll. The single roll flow pattern is generated by large gas injection, small SEN submergence depth and low casting speed. To maintain a stable double-roll flow pattern, which is often optimal, the argon should be kept safely below a critical level. The chosen optimal nozzle had 45mm inner bore diameter, downwards 15$^o$port angle, and 0.44 port-to-bore area ratio. The pointed bottom SEN generates smaller level fluctuations at the meniscus, larger impingement pressure, and deeper impingement than the recess-bottom SEN. The industrial measurement verifies that the recess-bottom SEN produces cleaner steel than the pointed-bottom SEN. Numerical simulation shows that on occasion, even large bubbles can penetrate deeply and be entrapped through the bottom outlet. This is more likely for 1mm bubbles than for 5mm bubbles. Due to the turbulent fluctuations, the motion of the bubbles in the mold is very random and sometimes asymmetrical. Mass balances of inclusions in the steel slag from slag and slab measurements shows that around 20% inclusions are removed from the steel into the mold slag. However, entrainment of the mold slag itself is a critical problem. Inclusions in the steel increase two-fold during ladle changes,. Slabs cast during the start and end of a sequence have the most inclusions.

## References

1) K. I. Afanaseva and T. P. Iventsov: *Stal*, (1958), **18**(7), 599.
2) N. T. Mills and L. F. Barnhardt: *J. of Metals*, (1971), **23**(11), 37.
3) N. T. Mills and L. F. Barnhardt: *Open Hearth Proceedings*, TMS-AIME, (1971)**, 54**, 303-315.
4) J. Szekely and R. T. Yadoya: *Metall. Trans. B*, (1972), **3**(5), 2673.
5) L. J. Heaslip and J. Schade: *Iron and Steelmaker (ISS Transactions)*, (1999), **26**(1), 33.
6) L. J. Heaslip, I. D. Sommerville, A. McLean, L. Swartz and W. G. Wilson: *Iron and Steelmaker (ISS Transactions)*, (1987), **14**(8), 49.

7) D. Gupta, S. Subramaniam and A. K. Lahiri: *Steel Res.*, (1991), **62**(11), 496.
8) D. Gupta, S. Chakraborty and A. K. Lahiri: *ISIJ Int.*, (1997), **37**(7), 654.
9) D. Gupta and A. K. Lahiri: *Metall. Mater. Trans. B*, (1996), **27B**(5), 757.
10) D. Gupta and A. K. Lahiri: *Metall. Mater. Trans. B*, (1994), **27B**(4), 695.
11) D. Gupta and A. K. Lahiri: *Ironmaking Steelmaking*, (1996), **23**(4), 361.
12) H. Tanaka, H. Kuwatori and R. Nisihara: *Tetsu-to-Hagane*, (1992), **78**(5), 761.
13) T. Teshima, J. Kubota, M. Suzuki, K. Ozawa, T. Masaoka and S. Miyahara: *Tetsu-to-Hagane*, (1993), **79**(5), 576.
14) M. Iguchi, J. Yoshida, T. Shimzu and Y. Mizuno: *ISIJ Int.*, (2000), **40**(7), 685.
15) Z. Wang, K. Mukai and D. Izu: *ISIJ Int.*, (1999), **39**(2), 154.
16) M. Iguchi and N. Kasai: *Metall. Mater. Trans. B*, (2000), **31B**(3), 453.
17) B. G. Thomas, L. J. Mika and F. M. Najjar: *Metall. Trans. B*, (1990), **21B**(2), 387.
18) J. Yoshida, M. Iguchi and S. Yokoya: *Tetsu-to-Hagane*, (2001), **87**(8), 529.
19) N. A. McPherson, in Steelmaking Conference Proceedings, **68**, eds., ISS, Warrendale, PA, (1985), 13-25.
20) H. Jacobi, H.-J. Ehrenberg and K. Wunnenberg: *Stahl und Eisen*, (1998), **118**(11), 87.
21) T. Wei and F. Oeters: *Steel Research*, (1992), **63**(2), 60.
22) M. Iguchi, Y. Sumida, R. Okada and Z. Morita: *Tetsu-to-Hagane*, (1993), **79**(5), 569.
23) S.-H. Kim and R. J. Fruehan: *Metall. Trans. B*, (1987), **18B**(2), 381.
24) I. Manabu, S. Yutaka, O. Ryusuke and M. Zen-Ichiro: *Tetsu-to-Hagane*, (1993), **79**(5), 33.
25) R. McDavid and B. G. Thomas: *Metall. Trans. B*, (1996), **27B**(4), 672.
26) T. Honeyands and J. Herbertson: *Steel Research*, (1995), **66**(7), 287.
27) M. Gebhard, Q. L. He and J. Herbertson, in Steelmaking Conference Proceedings, **76**, eds., Iron and Steel Society, (Dallas, TX, March 28-31, 1993), (1993), 441-446.
28) W. H. Emling, T. A. Waugaman, S. L. Feldbauer and A. W. Cramb, in Steelmaking Conference Proceedings, **77**, eds., ISS, Warrendale, PA, Chicago, IL, (1994), 371-379.
29) B. G. Thomas, X. Huang and R. C. Sussman: *Metall. Trans. B*, (1994), **25B**(4), 527.
30) J. Kubota, K. Okimoto, M. Suzuki, A. Shirayama and T. Masaoka: *ISC. The Sixth International Iron and Steel Congress. Vol. 3. Steelmaking I*, (1990), 356-363.
31) Y. Sasabe, S. Kubota, A. Koyama and H. Miki: *ISIJ Int.*, (1990), **30**(2), 136.
32) B. G. Thomas and L. Zhang: *ISIJ Internationla*, (2001), **41**(10), 1181.
33) L. Zhang and B. G. Thomas: University of Illinois at Urbana-Champaign, Report No. CCC200402, (2004).
34) Q. Yuan, T. Shi, B. G. Thomas and S. P. Vanka: *Computational Modeling of Materials, Minerals and Metals Processing, TMS*, B. Cross, Evans,eds., TMS (The Materials, Minerals, and Metals Society), Warrendale, PA, (2001), 491-500.
35) G. Abbel, W. Damen, G. de 燻 endt and W. Tiekink: I*SIJ*, (1996), 3**6,** S219.
36) L. Kiriha, H. Tosawa and K. Sorimachi: C*AMP-ISIJ*, (2000), 1**3,** 120.
37) L. Zhang and S. Taniguchi: I*nternational Materials Reviews*, (2000), 4**5(**2), 59.
38) H. Bai and B. G. Thomas: M*etall. Mater. Trans. B*, (2001), 3**2B(**2), 253.
39) H. Bai and B. G. Thomas: M*etall. Mater. Trans. B*, (2001), in press.
40) H. Bai and B. G. Thomas: M*etall. Mater. Trans. B*, (2001), 3**2B(**2), 269.
41) M. B. Assar, P. Dauby and G. Lawson, in Steelmaking Conference Proceedings, 8**3,** ISS, Warrendale, PA, (2000), 397-411.
42) P. H. Dauby, M. B. Assar and G. D. Lawson: R*ev. Met.*, (2001), 9**8(**4), 353.
43) T. Shi and B. G. Thomas: Continuous Casting Consortium at University of Illinois at Urbana-Champaign, Report No., (2001).
44) Z. Wang, K. Mukai, Z. Ma, M. Nishi, H. Tsukamoto and F. Shi: I*SIJ Int.*, (1999), 3**9(**8), 795.
45) Q. Yuan, B. G. Thomas and S. P. Vanka, in ISSTech2003 Conference Proceedings, ISS, Warrandale, PA, (2003), 913-927.
46) L. Zhang and B. G. Thomas: I*SIJ Internationla*, (2003), 4**3(**3), 271.
47) I. R. Lee, J. Chai and K. Shin, in 71th Steelmaking Conference Proc, 7**1,** eds., ISS, Warrendale, PA, (1988),
48) L. Zhang, B. G. Thomas, K. Cai, L. Zhu and J. Cui, in ISSTech2003, eds., ISS, Warrandale, PA, (2003), 141-156.